Applied Clay Science 212 (2021) 106223

Contents lists available at ScienceDirect

Applied Clay Science

journal homepage: www.elsevier.com/locate/clay

SEM-EDX study of bentonite alteration under the influence of cement alkaline solutions

Daniel E. González-Santamaría [a,*], Ana Justel [b], Raúl Fernández [a], Ana Isabel Ruiz [a], Alexandra Stavropoulou [c], Juan Diego Rodríguez-Blanco [c], Jaime Cuevas [a]

[a] *Department of Geology and Geochemistry, Faculty of Sciences, Autonomous University of Madrid, Cantoblanco, 28049 Madrid, Spain*
[b] *Mathematics Department, Faculty of Sciences, Autonomous University of Madrid, Cantoblanco, 28049 Madrid, Spain*
[c] *Department of Geology, School of Natural Sciences, Trinity College Dublin, Dublin 2, Ireland*

ARTICLE INFO

Keywords:
Bentonite
Alkaline perturbation
SEM-EDX
Cement
Engineered barrier system

ABSTRACT

Bentonite is a key barrier for the isolation of high-level radioactive waste within Deep Geological Repository. However, bentonite may be altered by contact with cementitious materials and their alkaline pore fluids. This study offers an extensive morphological and semi-quantitative characterization of the bentonite surface exposed to three types of alkaline pore fluids released by different cement-based materials. The bentonite surfaces were studied using a thorough scanning electron microscopy exploration and analysed using an energy-dispersive X-ray detector (SEM-EDX). In addition, statistical, element mappings, X-ray diffraction and infrared spectroscopy analyses were performed. The aim was to have a picture of the morphological and chemical alterations of bentonite at very early stages in accordance with the integrated approach necessary to address bentonite stability in the long-term. As a consequence of the reactivity, two types of morphologies stood out in the matrix of bentonite: platelets and coatings-like crusts characterized by their high Mg and Ca content. These alterations presented a different scope depending on the type of alkaline pore solution involved and suggested the precipitation of authigenic magnesium silicate hydrates (M-S-H) and/or trioctahedral clay minerals and Ca-carbonates. The knowledge of the performance of bentonite subjected to these alkaline solutions can help in the evaluation of the most suitable cement-based materials to be used next to bentonite.

1. Introduction

Bentonites are one of the selected materials for the isolation of high-level radioactive waste (HRLW). The main designs of Deep Geological Repositories (DGR) envisage their use as backfill and sealing material due to their buffer chemical properties and swelling ability (Tournassat et al., 2015; Gómez-Espina and Villar, 2016; Kaufhold and Dohrmann, 2016). The compacted bentonite will be located next to the canister that holds the HRLW in the Engineered Barrier System (EBS) (Sellin and Leupin, 2013; Ewing et al., 2016; Apted and Ahn, 2017; Norris, 2017; Turrero and Cloet, 2017) and must ensure the waste isolation until the radioactivity decays after 10^4–10^5 years. EBS designs in clayey or crystalline host rocks include the use of large volumes of cementitious materials as a sealing plug, and to support the galleries that house the EBS at over 400 m in depth. However, cement-based materials produce highly alkaline pore fluids in contact with groundwaters, which will reach the bentonite barrier modifying its properties (Savage et al., 2007; Dauzeres et al., 2010; Savage, 2014). To minimize these perturbations the so-called low-pH cement materials (pH $<$ 11) have been studied to be used instead of common high-pH cementitious materials (pH $>$ 12) (García Calvo et al., 2010; Lothenbach et al., 2012; García Calvo et al., 2013; Dauzères et al., 2014). Several types of low-pH cement materials are characterized by the addition of finely ground silica (eg., silica fume), which virtually avoids the formation of portlandite and as a result, lower quantities of OH^- ions are release into pore waters (Taylor, 1997). This allows pH to drop to values lower than high pH cementitious materials. It has been reported that low-pH cement-based materials have negligible effects on clay structures (Berner et al., 2013; Cuevas et al., 2016). Additionally, the hyperalkaline solutions provided by high-pH cement produce dissolution of silica and transformation of the smectites from bentonite. This reactivity would lead to a larger modification of the bentonite properties which could have negative effects e.g., reduction of swelling, adsorption capacity or clogging porosity (Ramírez et al., 2002; Gaucher and Blanc, 2006; Savage et al., 2007) and reduce

---

* Corresponding author.
E-mail address: daniel.g.santamaria@uam.es (D.E. González-Santamaría).

https://doi.org/10.1016/j.clay.2021.106223
Received 12 April 2021; Received in revised form 17 July 2021; Accepted 19 July 2021

the interchange of cations with clay. In contrast, positive effects have also been reported e.g., the development of a protective film, which would diminish the deterioration of the cementitious material (Mäder et al., 2017; Cuevas et al., 2018; Fernández et al., 2018).In addition, new phases can be formed, in this respect, Ca and Mg neogenic phases like Al tobermorite-type calcium silicate hydrates (C-A-S-H) and calcite have been found. Both phases were observed in batch experiments (Fernández et al., 2016) and Underground Research Laboratories (URL) as the Grimsel Test Site (GTS, Switzerland) (Blechschmidt and Vomvoris, 2010). The Ca and Mg-rich phases have been found in the concrete, in the concrete/clay interfaces (Jenni et al., 2014; Lerouge et al., 2017; Mäder et al., 2017) and/or in the clay (Fernández et al., 2017; Fernández et al., 2018). Additionally, authigenic Mg minerals and Ca-carbonates have been reported in clayey environments subject to alkaline solutions (Bristow and Milliken, 2011; Shimbashi et al., 2018). However, the structures of Mg-phases and C-A-S-H are difficult to characterize because of their complex structure and crystal chemistry (Nonat, 2004; Roosz et al., 2015; Nied et al., 2016). To date, several authigenic Mg silicates have been proposed: chlorite-like phase, brucite, Mg-Clays as 1:1 serpentine type or 2:1 trioctahedral smectites, magnesium silicate hydrates (M-S-H) (Cuevas et al., 2018; Fernández et al., 2018; Shimbashi et al., 2018). These phases precipitate in a thin surface layer mixed with the existing clay minerals present in bentonite, which makes it difficult to isolate for proper characterization. Bearing in mind that the design of EBS must be optimised to ensure its stability in the long term (IAEA, 2012), it is necessary to achieve a complete knowledge of its evolution from the early stages.

In this sense, to assess the bentonite regarding the neogenic Ca-Mg phases formed therein, the most common analytical techniques used are random powder X-ray diffraction (XRD) (which consist of aleatory powder mount that allows the characterization of detailed features like the dioctahedral or trioctahedral character by 060 reflections; Moore and Reynolds Jr, 1989); nuclear magnetic resonance (NMR); transmission electron microscopy (TEM) or Fourier transform infrared (FT-IR) spectroscopy analyses. However, the problem that arises from short-term and small-scale experiments is the very limited presence of newly-formed phases and therefore, the detection, identification and characterization of altered regions is highly challenging. Moreover, some analytical techniques require further samples preparation, which lengthens the experimental procedures being a drawback to carry out numerous analyses. In this respect, scanning electron microscopy (SEM) analysis is a faster tool and requires simple preparations of the samples, however is not able to determine structures. SEM observations allow defining morphologies at the μm size range, such as the aggrupation of particles to form aggregates. In addition, this technique makes it possible to distinguish their boundary relationships, particle arrangements (texture) and growth mechanics (Bohor and Hughes, 1971). SEM equipment can be coupled to an energy-dispersive X-ray (EDX) detector providing a semi-quantitative chemical element composition of the areas analysed. Nonetheless, the spatial resolution concerning chemical analysis is still limited to ~1 μm by beam spreading despite the greater depth of focus and higher resolution reachable by SEM (Reed, 2005; Goldstein et al., 2017); therefore, nanometre (nm) particles cannot be well characterized and they are critical for identifying the different types of clay minerals and thus the existence of alteration processes.

Clays exhibit particular morphologies and sizes that depend on the conditions of growth, like pH of the pore solutions, temperature or chemical composition; therefore, by changing a specific parameter like the alkaline pore solution, different experiments conducted under the same conditions can be compared. Furthermore, by combining the statistical analysis of morphologies with the chemical data, it is possible to infer the processes that resulted in the early perturbations of FEBEX-bentonite. In this context, this work presents an extensive SEM-EDX characterization of bentonite after its interaction with the alkaline solutions coming from three different cement-based materials. Therefore, this study aims to shed light of the bentonite alterations induced by Ordinary Portland Cements (OPC), focusing on the morphologies formed and their chemical composition after alteration. Owing to the limitation of the spatial resolution of the electron beam, this approach has been reinforced with statistical tools and complemented with element mappings, grazing incidence X-ray diffraction (GI-XRD), XRD θ/2θ scans, and FT-IR analyses.

2. Materials and methods

2.1. FEBEX-bentonite

The FEBEX-bentonite was obtained from Almería (Spain), specifically from Cortijo de Archidona deposits (Caballero et al., 1985; Caballero et al., 2005). The main characteristics are its high smectite content, mainly montmorillonite (92 ± 3 wt%) with minor quantities of quartz (2 ± 1 wt%), plagioclase (3 ± 1 wt%), K-feldspar (traces), cristobalite-tridymite (2 ± 1 wt%) and trace contents in accessory minerals such as carbonates (mainly calcites), sulphates, pyrite and apatite. The FEBEX-bentonite presents a high cation exchange capacity (~100 cmol(+)/kg) with an exchangeable cation distribution of approximately one third in Na^+, Ca^{2+} and Mg^{2+} and a total and BET external specific surface area of ~725 m^2/g and 62 m^2/g, respectively; the first one corresponds to the total surface area and involves the internal and external surfaces. On the other hand, the internal surface area computes the surface of basal planes of the montmorillonite while the external only those surfaces surrounding the discrete stacked packets of clay mineral (ENRESA, 2002; Fernández et al., 2004).

2.2. Experimental configuration and alkaline solutions

Alkaline solutions were originated by the injection of a granitic groundwater solution through cylindrical columns composed of cement mortars faced to bentonite, which was uniaxially compacted with its hygroscopic water content (13%) at nominal dry density of 1.60 g/cm^3. The contact area between the cement mortar and bentonite was separated by a polytetrafluoroethylene (PTFE) membrane (diameter: 0.45 μm), only allowing alkaline fluids and colloids to cross it and reach the bentonite. This set-up avoided its contamination with cement scraps, facilitating the separation of materials and subsequent access to the bentonite surface once the experiments concluded. Fig. 1 illustrates the device (i.e., transport cells) used, which simulate at very small scale interaction conditions envisaged for an EBS designed according to the DGR crystalline rock concept (Ewing et al., 2016) as well as the conditions implemented in the Full-scale Engineered Barrier EXperiment (FEBEX)-project (ENRESA, 2006). A deeper explanation of the experimental configuration, as well as details of the materials and methods used, can be found in González-Santamaría et al. (2020b).

The first type of leachate consisted of a fluid with a relatively low pH (<11) provided by a low-pH cement mortar. This type of cementitious material was made by mixing CEM-I OPC and silica fume. The other two alkaline solutions (pH >12) were provided by high-pH cement mortars made with CEM-I and CEM-II A-L OPC (these types of cement mortars will be referred to as CEM-I and CEM-II) where the last one highlights by the presence of 10% extra limestone addition with a grain size around 1 μm. The three types of experiments drawn (hereinafter named LpH-experiments, CEM-I-experiments and CEM-II-experiments) were run at isothermal conditions (23 ± 2 °C) in duplicate, for 6 and 18 months. Therefore, a total of 12 surfaces of bentonite were studied. Additionally, unaltered bentonite samples were analysed to have a reference.

2.3. SEM-EDX characterization

Once experiments were finished, several slices were cut with a diamond thread cutter from the bentonite surface. The flat samples of clay were dried in a vacuum chamber at 25 °C with P_2O_5 dehydrated atmosphere until 10^{-4} Pa. Previously to SEM-EDX analysis a Quórum

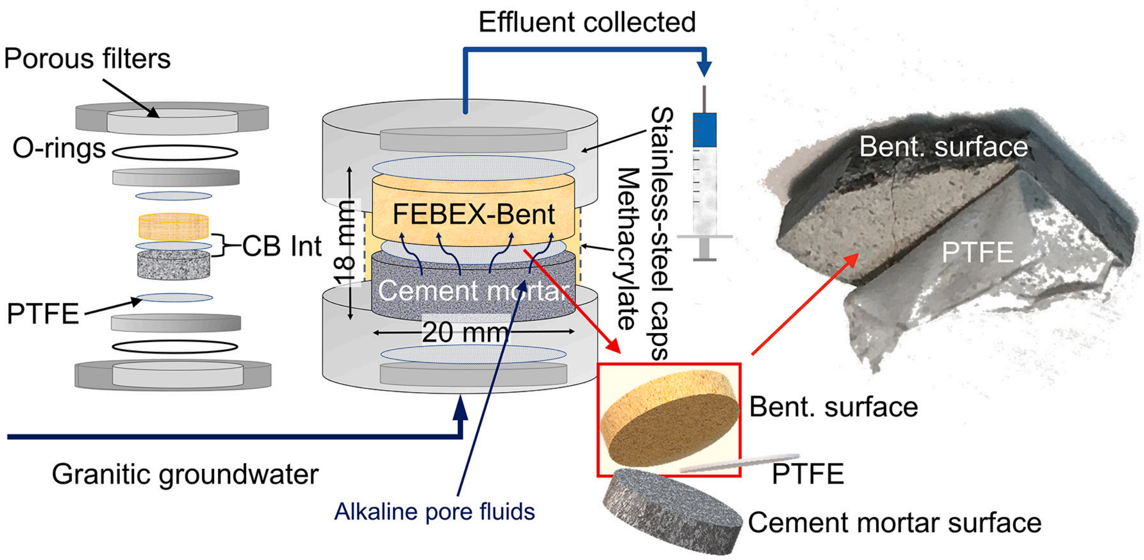

Fig. 1. Transport cells containing the surface of bentonite exposed to alkaline pore fluids provided by cement mortars. A methacrylate piece seals the FEBEX-bentonite and cement mortars, which are separated by a polytetrafluoroethylene (PTFE) membrane and encased in open stainless-steel caps. Two porous filters enable water transport at both materials ends. On the right of the figure, a photograph of a slice of the surface of bentonite is shown. CB int: cement mortar–bentonite interface, Bent: bentonite. Figure modified from González-Santamaría et al. (2020b).

sputter metallisation, Q150T-S, was carried out for Au plating.

Based on magnifications of the analyses and morphologies found, four groups across all samples were established: areas (homogeneous regions analysed at 45× magnifications), matrices (spots and minor regions analysed at high magnifications, >2000–3000×), platelets (morphologies characterized by crinkly, ridged, honeycomb-like texture) and crusts (morphologies without well-defined shapes developing as deposits). Analyses of areas and matrices allowed to set the overall chemical composition of the surface of bentonite samples once exposed to alkaline solutions. Additionally, spot μm-size analyses were performed over the platelets and crusts with the aim to assess and compare these morphologies throughout the different experiments and assess their chemical composition. The equipment used was a Hitachi S-3000 N scanning electron microscope (Hitachi Ltd., Tokyo, Japan) coupled to an INCAx-sight Oxford Instruments™ energy dispersive X-ray analyser (Oxford Instruments, Oxon, UK). The equipment operating under high vacuum conditions using an accelerating voltage of 20 keV, livetime of 40 s, a working distance from 15.0 to 18.5 mm and a beam current of 300 mA. The EDX quantification was performed by means of internal standard semi-quantitative analysis (supplementary file. S6). For EDX semi-quantification, the statistical quality of the measurements was better than 10%. In terms of spots analysis performed over the matrix, platelets and crusts, the atomic ratios were lower than 10–15% deviation considering the influence of the phases surrounding the electron beam (e.g., Si, Al phases and carbonates) (more details are available in Cuevas et al., 2018; González-Santamaría et al., 2018).

2.4. Statistical survey

The amount of data (>300 analysis) from SEM-EDX allowed carrying out a statistical survey. This study tested the homogeneity of chemical composition among the type of groups (areas, matrices, platelets, and crusts) and between the type of experiments (LpH, CEM-I and CEM-II-experiments) by means of a two-factor ANOVA interaction model. Individual factor effects and/or interactions are considered statistically significant if the *p*-value was <0.05. When any of the hypotheses of equal means is rejected, the corresponding multiple comparisons were made with Bonferroni correction with an overall significance level $\alpha = 0.05$. To run the tests, oxygen was removed from the chemical analysis and data were normalized to 100%. In the second stage, the variables Mg, Si, Al and Ca from the chemical composition were jointly examined by Principal Components Analyses (PCA). Two Principal Components (PC1, PC2) were extracted according to their eigenvalues. In addition, Pearson correlation coefficients were calculated for each pair of Mg, Ca, Si, K and Fe. OriginPro® 2017 (version 9.4) and IBM SPSS Statistics software (version 26) were used for the statistical analyses.

2.5. Ternary diagrams

Two types of ternary projections were built to approach the type of phase present on the surface of bentonite. The analytical data acquired from EDX analysis were presented as atomic proportions (% moles of element) and were transformed into an MR^{3+}–$2R^{3+}$–$3R^{2+}$and M^{+}–4Si–$3R^{2+}$ ternary plots where M^{+} component represents the charge of exchangeable cations: $Na^{+}+K^{+}+2Ca^{2+}$; 4Si component is equal to Si/4; $2R^{3+}$ component represents $(Al + Fe - M^{+})/2$; and $3R^{2+}$ represents Mg/3.

2.6. Structural formulas

Data to calculate the structural formulas were based on the EDX semi-quantitative analysis and were approached assuming a 2:1, 2:1:1 and 1:1 clay mineral arrangements in a $O_{10}(OH)_2$, $O_{10}(OH)_8$ and $O_5(OH)_4$ anion basis, respectively. The procedures applied for the assignment of the cations position were as follows: for 2:1 structures, (i) Si^{4+} was assigned to the tetrahedral sheet, (ii) the charge deficiency present in the tetrahedral sheet was completed with Al^{3+} cations until the tetrahedral site occupancy was equal to 4 –and 2 for 1:1 structural formulas– (iii) the remaining Al^{3+} as well as Fe^{3+} were assigned to the octahedral sheets for a total octahedral charge of +6 (Moore and Reynolds Jr, 1989; Bleam, 2017). All Fe at.% detected was counted as Fe^{3+}. (iv) If a charge deficit occurred, the octahedral sheets were balanced with Mg^{2+}. (v) Cations such as Ca^{2+}, Na^{+} and K^{+} were allocated in the interlayer sites where it was appropriate. In the case of 2:1:1 structures, Al^{3+} was assigned to the octahedral sheet from interlayer site and was complete with Mg^{2+} until the site occupancy was equal to three (Bouchet et al., 2002). When the Ca content was too high it was interpreted as a result of the influence of other phases different to clay minerals so it was removed with the aim to calculate a plausible structural formula.

2.7. *Complementary analyses*

To complement and support the survey, element mappings, XRD θ/2θ scans, GI-XRD and FT-IR analyses were conducted on the very flat bentonite surfaces.

2.7.1. *Element mappings*

Element mappings were obtained from the surface planes of the bentonite to assess the distribution of elements and their relationship with the groups established. Additionally, element mappings were performed from the edge of the bentonite inwards to observe the scope of the alterations further away from the edge of the surface plane (see section 3.2. Fig. 6g and h). The transversely cut sections were freeze-dried, embedded in epoxy resin and finally polished up to 2500 grit sheet sandpaper just before each SEM-EDX session. Maps and high-resolution SEM images were acquired using a SEM-EDS Tescan MIRA XMU FE-SEM model. The equipment operating under high vacuum conditions using an accelerating voltage of 20 keV and at 18.5 mm working distance; the beam current of 300 mA was fitted with a 150 mm^2 Energy Dispersive Spectroscopy (EDS) Oxford Instrument Detector. The maps were generated with a resolution between 1024 and 2048 pixels in the *x* dimension, the analyses were performed using a pixel dwell time of 2000–3000 μs, and frames were averaged for 8–12 h. For transversally maps the total measurement time reached 40 h. Elemental compositional maps were constructed using the Oxford Instruments AZtec® analysis software.

2.7.2. *XRD θ/2θ scans and GI-XRD analyses*

A total of ten XRD analyses were obtained for each type of experiment on the flat bentonite surfaces. The analyses were carried out either using XRD θ/2θ scans and GI-XRD 0.5° fix incidence angle configurations at 6 and 18 months after the first interaction between the alkaline pore fluids and bentonite. All analyses were done in duplicate, XRD θ/2θ scans and GI-XRD (were also performed in a reference bentonite sample. The analyses were obtained using an X'Pert PRO PANalytical diffractometer with parallel beam optics, secondary monochromator and Xenon detector. An angular range from 3 to 70° 2θ was used with an 0.04° angular step (2 s time). The voltage and intensity of the operated X-ray Cu tube were 45 kV and 40 mA. The database used to assess the diffractograms was the ICDD PDF-4 + .

2.7.3. *FT-IR analysis*

FT-IR analyses were obtained using a Nicolet 6700 FT-IR spectrometer (Thermo Fisher Scientific, Waltham, MA, USA) in transmission mode with a deuterated tri-glycine sulphate (DTGS) KBr detector and recording over the Mid-Infrared region spectral range (4000–400 cm^{-1}). For these analyses, 2 mg of surface bentonite was scraped and grinded in a Retsch RM200 mortar grinder with a pestle of agate and mixed with 100 mg of KBr.

3. Results

3.1. *SEM micrographs and EDX analyses*

3.1.1. *Reference FEBEX-bentonite*

The exploration by SEM-EDX of the unaltered bentonite section showed homogeneous surfaces at low magnifications (45× areas), while roughed matrices and platelets shapes dominated the section studied at higher magnifications (>3000×, Fig. 2).

The chemical composition acquired from the areas, matrices, platelets and crusts (Table 1) were consistent with the bentonites from Cabo de Gata deposits (Huertas et al., 2001; Fernández et al., 2004; Caballero

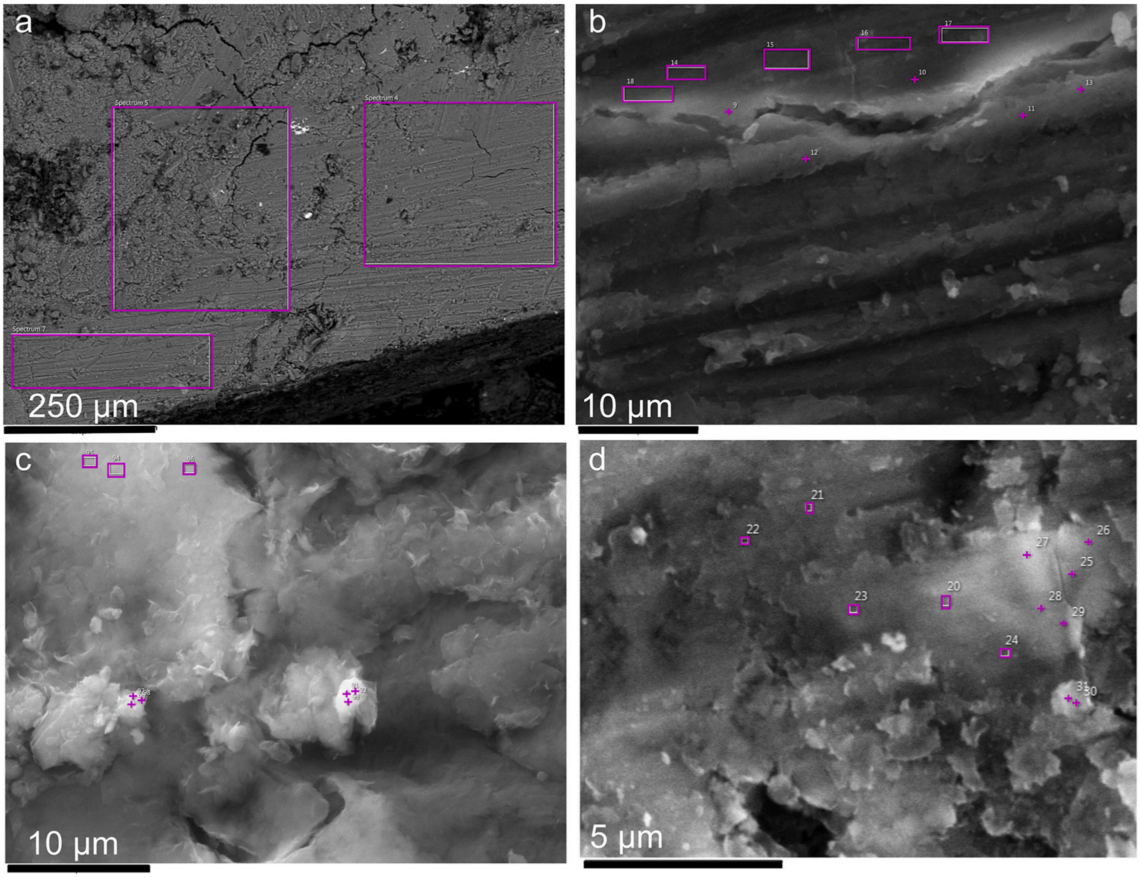

Fig. 2. Secondary Electron (SE) images of the reference bentonite sample. a) areas analysed, b) matrices analysed, c) and d) platelets analysed.

Table 1
Mean of the EDX analyses of reference FEBEX-bentonite.

Areas	Scale:	<1 mm	Matrices	Scale:	10 μm	Platelets	Scale:	10 μm
Atomic%	X	± Ex	Atomic%	X	± Ex	Atomic%	X	± Ex
O	67.67	0.12	O	65.56	0.47	O	67.69	0.72
Na	0.74	0.04	Na	0.74	0.01	Na	1.06	0.14
Mg	2.30	0.08	Mg	2.81	0.05	Mg	2.83	0.16
Al	7.38	0.15	Al	8.64	0.08	Al	7.84	0.12
Si	19.53	0.40	Si	20.70	0.32	Si	19.06	0.50
K	0.33	0.03	K	0.11	0.00	K	0.19	0.02
Ca	0.87	0.11	Ca	0.69	0.03	Ca	0.67	0.02
Fe	1.12	0.37	Fe	0.76	0.03	Fe	0.66	0.08
Mg/Si	0.12	0.00	Mg/Si	0.14	0.00	Mg/Si	0.15	0.01
No. analyses	3		No. analyses	10		No. analyses	8	

X: average values, ± Ex: standard error of the mean.

et al., 2005).

3.1.2. LpH-experiments

The SEM-EDX analyses of the bentonite surface planes exposed to the low pH pore fluids revealed the presence of crust shapes. These crusts showed a gel-like morphology deposited on the surface of the matrix (Fig. 3b, c and f). In addition, platelets morphologies were found with a crinkly, ridged, honeycomb-like texture characteristic of the smectites group (Fig. 3d and e). The SEM imaging carried out at the highest magnifications allowed the observation of the basic textures found in the altered bentonite. (Fig. 3b, c, d, e and f).

The chemical elemental analysis of areas, matrices, platelets as well as crusts revealed higher Mg/Si ratios than the reference bentonite (Table 2), suggesting the alteration of the bentonite surfaces under the low-pH alkaline solution.

3.1.3. CEM-I-experiments

Bentonite exposed to CEM-I pore fluids stood out by the wide presence of platelets. These platelets consisted of a mixture of thin flakes bounded through face-edges contacts rather than face-face contacts (Fig. 4). It can be appreciated that the thickness of the platelets was shorter than 1 μm.

CEM-I-experiments revealed Mg-rich crusts and were observed in the form of strips similar to those found in LpH-experiments, but EDX analyses showed the highest Mg at.% (Tables 3 and 4, section 3.1.4).

3.1.4. CEM-II-experiments

The texture of the areas and matrices of the CEM-II experiments was different compared to the LpH and CEM-I-experiments (Fig. 5). CEM-II-experiments were notable for the widespread presence of Ca and Mg-rich crusts, which consisted of blocks instead of strips (Table 4).

3.2. Element mappings

EDS maps were obtained in bentonite samples subjected to high-pH alkaline fluids to characterize the areas with the highest alteration previously observed (González-Santamaría et al., 2020b) (Fig. 6). Elemental mapping showed Mg-rich regions associated with the platelets and crusts morphologies (Fig. 6a, d, c, d). Ca concentrations were found scattered in isolated sites and mostly associated with crust shapes (Fig. 6b, d). Element mappings of Ca and Mg (Fig. 6e, f) acquired in the same scanned grid (region) suggested that both elements precipitated separately. Furthermore, Fe was commonly found associated with platelets (Fig. 6c).

Analyses of the transversally cut sections showed an increase of Mg towards the surface plane (Fig. 6g, h) revealing its accumulation in the first ~50 μm from the interface.

3.3. EDX-statistical survey

3.3.1. Pearson correlation coefficient

The scattering matrix (see the supplementary file, Fig. S1) indicates the relationship between pairs of chemical elements when they are crossed in the triangles. Mg showed a strong negative correlation with Si being clearer in CEM-I and CEM-II-experiments (Fig. S1, upper triangle) and platelets morphologies (Fig. S1, lower triangle). Similarly, Al and Ca suggested a weak negative correlation with Mg across groups and types of experiments.

3.3.2. Two-factor ANOVA model

The two-factor ANOVA model showed a significant interaction between the type of experiments and groups (p-value <0.05) and proved that the different chemical compositions significantly depend on both factors. The model showed that i) the three alkaline solutions affected the chemical composition of the bentonite surface differently and ii) morphologies conditioned the chemical composition observed by SEM-EDX (Fig. 7). Platelets and crusts showed marked differences, either among the three types of experiments or among the groups. Multiple comparisons of the means with Bonferroni correction (supplementary file, S2) did not provide statistically significant differences (p-value >0.05) between areas and matrices in all types of groups and therefore, both approaches would be representative of the bulk of bentonite.

The Mg perturbation was larger in CEM-I-experiments where platelets and crusts reached the highest values. For crusts, the Mg content also increased in LpH-experiments. Ca was very low in LpH and CEM-I-experiments, but CEM-II-experiments presented large Ca crust morphologies. Regarding Si, it was observed a marked decrease in crust morphologies from CEM-II experiments, where the Si decrease was counteracted by Ca suggesting the precipitation of Ca-phases. Al in LpH-experiments was higher in platelets, in agreement with the lower Mg content in the octahedral sheet, characteristic of dioctahedral montmorillonite originally present in bentonites then, indicated a lesser alteration of bentonite. Fe and K presented the lowest at.% (0.5–1) and was higher in platelets from LpH-experiments.

3.3.3. Principal component analysis: PCA

PCA was performed considering separately the type of experiment and groups. The results are depicted as biplots (supplementary file, Fig. S3), which allow to easily relate chemical composition with the type of experiments or groups through eigenvectors (arrows) and scores (dots). Regarding scores of the three types of experiments (Fig. S3a), Mg is more relevant in those performed with CEM-I while Ca had more weight with CEM-II-experiments. A description of the extracted eigenvectors and the eigenvalues of the correlation matrix (percentage of variance) can be found in the supplementary file, S4.

Analysing the relationship between chemical compositions and groups within each type of experiment separately (Fig. S3b, S3c, S3d), Mg in LpH-experiments had the highest weight, and their levels were

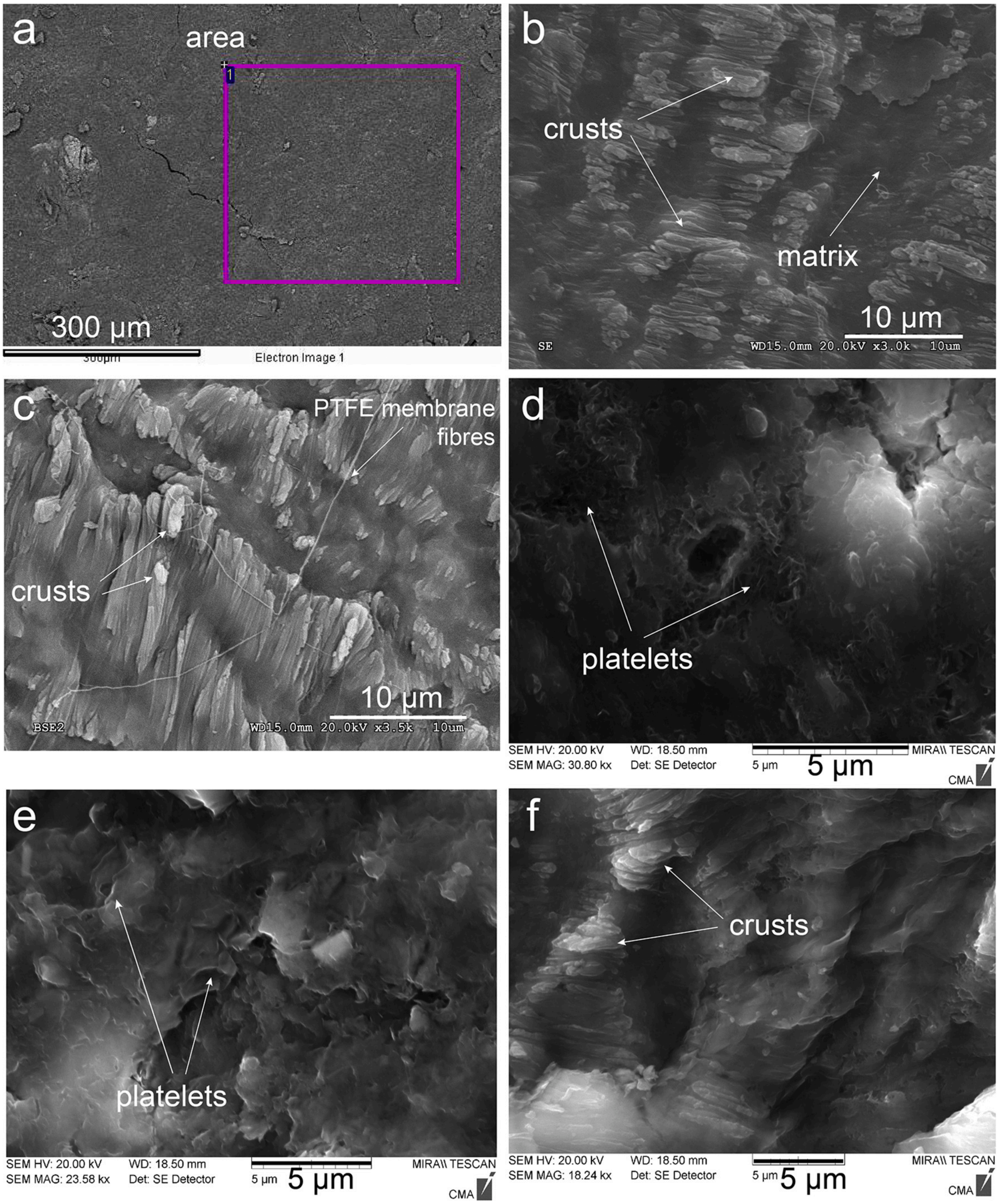

Fig. 3. SEM micrographs from the surface planes of bentonite exposed to low-pH alkaline fluids. a) Back Scattered Electron (BSE) image representative of areas, b) SE image of crusts and matrices. c, f) SE image of striped crusts. d, e) SE image of platelets.

associated with crust morphologies while the lowest was linked to platelets. However, in CEM-II the opposite was observed: higher levels of Mg were linked to platelets while the crust morphologies were markedly associated with Ca (Fig.S3c). CEM-I-experiments highlighted due to Mg was largely associated with platelets and presented the greatest loading values. In summary, Ca in CEM-II-experiments showed a strong relationship with crust morphologies in the PC1 corroborating that these morphologies were mainly constituted by Ca, but in LpH-experiments by Mg. On the other side, Mg in CEM-I was associated with platelets suggesting that these morphologies presented visible Mg increase. Finally, Si and Al were related to matrices and areas throughout all experiments.

3.4. *Ternary diagrams*

Ternary diagrams were built to differentiate di- and trioctahedral clay minerals (Velde, 1985; Bouchet et al., 2002; Meunier, 2005) (Fig. 8) as well as to assess the possible presence of neogenic formed phases. The domains of reference minerals and the characteristic areas corresponding to trioctahedral smectites have been shaded according to Velde (1985). Generally, a trend of plots towards the 3R^{2+} component was observed in all experiments. Regarding LpH-experiments, the platelets morphologies suffered a slight shift towards the 3R^{2+} component of the reference bentonite composition and unaltered montmorillonite present in the FEBEX-bentonite (Mt-F). On the contrary, most of the spots corresponding to areas, matrices and crust morphologies, were positioned

Table 2
EDX analyses of the LpH-experiments.

Areas	scale: <1 mm		Crust	scale:	10 μm	Matrices	scale:	10 μm	Platelets	scale:	5 μm
Atomic.%	X	± Ex	Atomic.%	X	± Ex	Atomic.%	X	± Ex	Atomic.%	X	± Ex
O	68.98	0.80	O	67.48	0.87	O	65.38	2.17	O	65.65	0.38
Na	0.25	0.02	Na	0.15	0.03	Na	0.26	0.05	Na	0.47	0.03
Mg	8.77	0.34	Mg	11.66	0.30	Mg	7.65	0.33	Mg	4.60	0.32
Al	4.82	0.36	Al	4.67	0.24	Al	6.46	0.62	Al	7.60	0.20
Si	15.80	0.14	Si	14.97	0.41	Si	18.62	1.30	Si	18.45	0.22
K	0.24	0.02	K	0.13	0.02	K	0.23	0.06	K	1.13	0.25
Ca	0.60	0.04	Ca	0.35	0.02	Ca	0.68	0.12	Ca	0.87	0.05
Fe	0.61	0.03	Fe	0.55	0.07	Fe	0.73	0.17	Fe	1.24	0.13
Mg/Si	0.56	0.02	Mg/Si	0.80	0.03	Mg/Si	0.41	0.02	Mg/Si	0.25	0.02
No. analyses	11		No. analyses	27		No. analyses	13		No. analyses	12	

X: average values, ± Ex: standard error of the mean.

further away. These last three groups were in the trioctahedral domain (Sm-tri) and/or in superimposed trioctahedral clay minerals (e.g., saponite). In CEM-I and CEM II-experiments, several points that correspond mainly with crusts and platelets morphologies stayed out of the ternary diagrams and were dismissed. Since these points did not fit well with the chemical composition of 2:1 clay minerals, they would correspond to other mineral phases or to a mixture of several phases rich in Ca and/or Mg.

The platelets from CEM-I-experiments overlapped with crust morphologies and showed a trend towards the $3R^{2+}$ component. In lots of cases, plots remained concentrated in the trioctahedral domain for all groups suggesting a change from di to trioctahedral structure, but some analyses of platelets morphologies were in the edge of the ternary projections due to the high influence of Ca computed by M^{+} component.

The CEM-II-experiments displayed more scattered plots and can be appreciated a trend of a considerable number of points towards the MR^{3+}/M^{+} component. This result agrees with the strong loading of Ca in the PC1 (Fig.S3d, X-axes) of PCA. Besides, it highlights the influence of Mg regarding the displacement of the data to the $3R^{2+}$ component as it has been shown for the PC2 (Fig. S3d, Y-axes) of PCA.

3.5. Structural formulas

The average structural formula of platelets and crusts for each type of experiment and reference bentonite was calculated based on the EDX analysis carried out and were fitted to 2:1, 2:1:1 and 1:1 clay minerals structures (Table 5). In this context, the coefficients of cations are sensitive to the presence of mineral admixtures, and charge calculation is sensitive to the presence of impurities (Czímerová et al., 2006). Besides, substantial deviations from the theoretical octahedral cation occupancy (from 2 to 3) could denote the presence of more than one phase (Elless, 1995) or indicate the presence of vacancies in 2:1 phyllosilicates (Lerouge et al., 2017). Accordingly, the analyses carried out that presented large deviations were excluded and read as indicative of the presence of other mineral phases and/or the existence of a mixture of phases. Exceptionally, a large spread of Ca was found in the case of CEM-II-experiments, this excess of Ca had to be excluded and then, the other chemical elements were normalized to 100% to adjust feasible structural formulas. Consequently, the Ca present in the interlayer was not possible to assign.

Focusing on the LpH-experiments, the structural formula of platelets was adjusted to a 2:1 dioctahedral smectite, similar to reference bentonite and thus, weak alteration occurred in agreement to results shown by the ternary diagrams and EDX analysis. The 0.65 charge per half unit cell (*X*) was close to the characteristic range of smectite (from 0.2 to 0.6; e.g., Brindley, 1980). Concerning the number of octahedral cations, is commonly accepted that dioctahedral smectites present between 2.00 and 2.22 values (Meunier, 2005; Christidis, 2006; Emmerich et al., 2009; Brigatti et al., 2013). Besides, occupancies from 2.22 to 2.88 indicate a mix of trioctahedral and dioctahedral smectites while trioctahedral smectites present sites occupancies from 2.88 to 3.00. Taking this into consideration, trioctahedral structures (2:1 rather than 2:1:1 because of low 2:1 sub-sheet octahedral occupancy) of LpH-experiments were found for the crust-like morphologies; therefore, these morphologies were indicative of an alteration process leading to new 2:1 tri-octahedral sheet silicates.

CEM-I-experiments showed greater Mg contents in the newly formed precipitates. For platelets, the presence of a 1:1 serpentine-like structure is feasible and, again 2:1:1 chlorite-like structure, although presented a good fit, also contain a low number of octahedral cations to fulfil this type of structure. For crusts, either 2:1:1 and 2:1 trioctahedral structures also showed a good fit. Several serpentine clay minerals can suffer isomorphic substitutions e.g., Lizardite (Grim, 1953; Dixon, 1989; Brigatti et al., 2013) and can be confused with chlorite and smectite. Therefore, to differentiate them, the analytical results showing (Fe + Mg)/Si ratios about 1.5 (characteristic of the serpentine group) were assigned to 1:1 serpentine-like structure (Shimbashi et al., 2018), while ratios about 0.5–0.8, and 0.9–1.3 were assigned to 2:1 smectite arrangement and 2:1:1 chlorite-like structure respectively.

CEM-II-experiments showed a good match for 2:1 trioctahedral smectites for platelets, and 2:1:1 chlorite-like structure in the case of crusts and once Ca was excluded.

3.6. XRD θ/2θ scans and GI-XRD analyses

Despite the fact that θ/2θ scans and GI-XRD 0.5° analytical techniques do not allow to identify separately areas, matrices, platelets and crusts, and cannot be related directly with morphologies, they provided valuable complementary information for a better interpretation of the EDX approach. (GI-)XRD analyses showed in the three types of experiments the presence of both di- and trioctahedral clay minerals on the surface of bentonite (supplementary file, Fig. S5a). In this regard, and as mentioned above, the 06 l reflection is useful to distinguish di- and trioctahedral clay minerals because d060-value is sensitive to the degree of occupancy and the size of cations in octahedral sheets (Brindley, 1980; Bouchet et al., 2002). The presence of trivalent cations as Al^{3+} leads to a lower 060 reflections between planes (1.49–1.51 Å) while divalent cations as Mg^{2+} leads to a higher 060 reflections between these planes (1.53–1.54 Å) hence, the wider reflections obtained in a 1.53 Å, 1.50 Å or 1.49 Å (more marked in CEM-I and CEM-II-experiments) suggested the precipitation of authigenic trioctahedral clay minerals coexisting with the dioctahedral clay minerals already present in the reference bentonite. Among diffractograms acquired in the LpH-experiments, bentonite displayed a reflection in a 7.4–7.6 Å after 18 months of exposure to the low-pH alkaline solution while CEM-I and CEM-II-experiments presented these reflections more regularly and earlier (at 6 months) indicating a further alteration of the bentonite exposed to high-pH pore fluids. These 7.4–7.6 Å d-values (002 reflections) and the reflections found in the 06 l indicated a neogenic mineral formation consistent with the several Mg-rich phases like M-S-

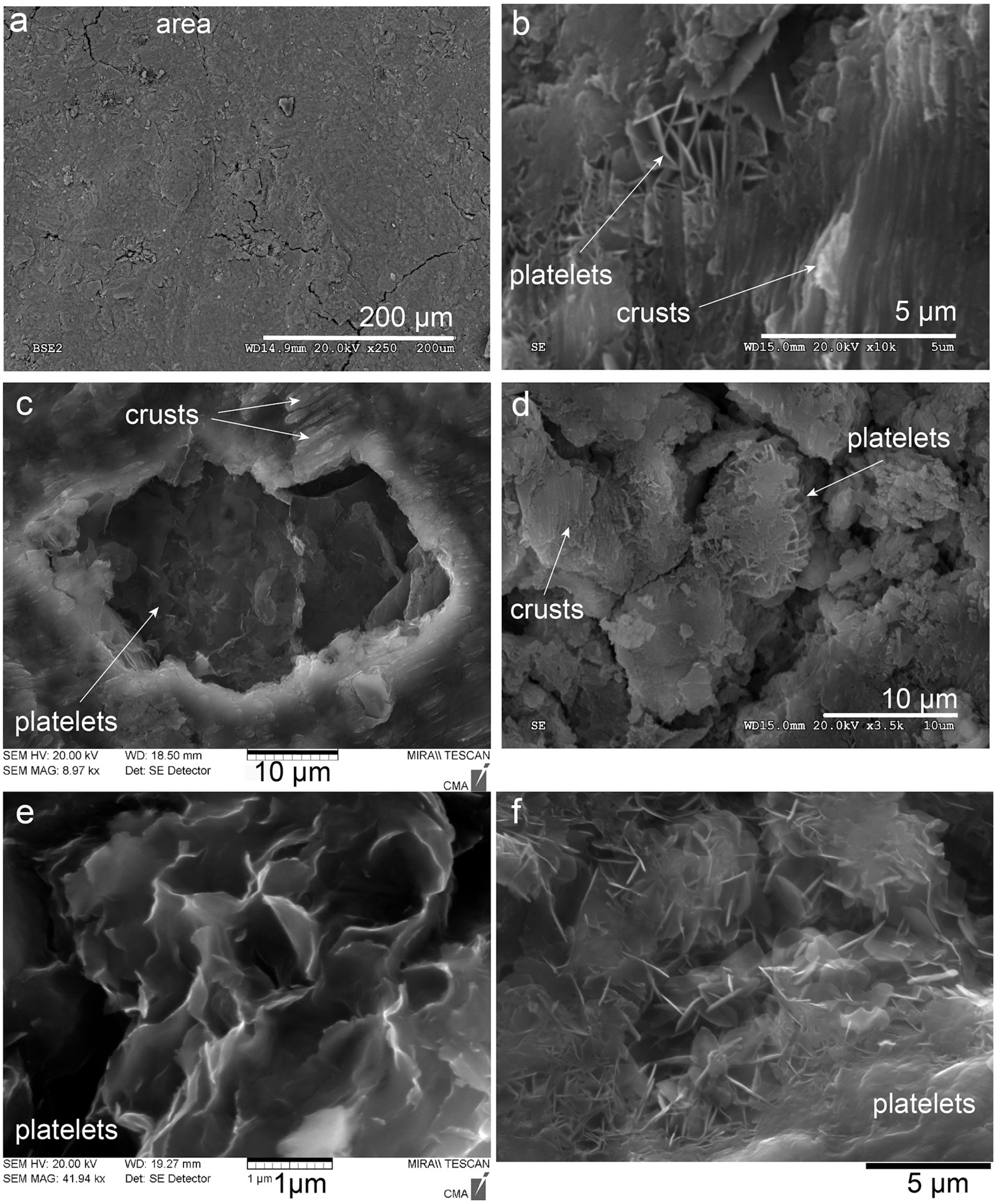

Fig. 4. SEM micrographs from the surface planes of bentonite exposed to high-pH alkaline fluids. a) BSE image of bentonite area. b, c, d, e) SE images of platelets and crusts. f) SE image of platelets like a honeycomb texture.

H, or brucite intercalated in the interlaminar space of montmorillonite or the precipitation of trioctahedral clay minerals. In fact, the 7.5, 3.7 and 2.4 Å reflections are consistent with a 1:1-type sheet silicate or a 2:1:1 superstructure of a 15 Å chlorite-like mineral (Fernández et al., 2013; Cuevas et al., 2018; Fernández et al., 2018; Shimbashi et al., 2018; González-Santamaría et al., 2020a). These observations are consistent with the number of octahedral cations estimated in some of the structural formulas (>2.22) suggesting the presence of trioctahedral clay minerals (section 3.5).

The characteristic calcite reflection at 3.03 Å d-values was detected in high-pH-experiments, particularity it was more developed in the CEM-II-experiments showing more intensity, being sharper and thus, suggested higher Ca-carbonate precipitation. This is consistent with the high content of Ca detected by EDX, mainly in crust morphologies. On the contrary, LpH-experiments did not present discernibly 3.03 Å calcite reflections and is coherent with the smaller amount of Ca detected by EDX in this type of experiment.

In summary, the (GI-)XRD study supported the previous results concerning structural formulas, ternary diagrams and statistical analysis arisen from EDX analysis.

3.7. FT-IR spectra

Infrared spectroscopy was performed in representative bentonite

Table 3
EDX analyses of the CEM-I-experiments.

Areas	scale: <1 mm		Crusts	scale:	< 5 μm	Matrices	scale:	<10 μm	Platelets	scale: <10 μm	
Atomic.%	X	±Ex	Atomic.%	X	± Ex	Atomic.%	X	± Ex	Atomic.%	X	± Ex
O	68.44	2.99	O	70.16	2.23	O	67.79	0.35	O	65.19	0.46
Na	0.16	0.03	Na	0.03	0.02	Na	0.06	0.01	Na	0.06	0.01
Mg	9.97	0.54	Mg	11.76	0.91	Mg	11.03	0.29	Mg	13.71	0.19
Al	5.43	0.30	Al	4.41	0.62	Al	5.59	0.14	Al	5.51	0.08
Si	14.41	0.73	Si	12.17	1.67	Si	14.22	0.19	Si	13.67	0.26
K	0.27	0.02	K	0.18	0.10	K	0.25	0.04	K	0.24	0.02
Ca	0.57	0.08	Ca	0.19	0.06	Ca	0.30	0.01	Ca	0.47	0.02
Fe	0.71	0.05	Fe	0.48	0.17	Fe	0.69	0.04	Fe	1.01	0.08
Mg/Si	0.70	0.04	Mg/Si	1.17	0.37	Mg/Si	0.78	0.10	Mg/Si	1.05	0.03
No. analyses	23		No. analyses	13		No. analyses	32		No. analyses	129	

X: average values, ± Ex: standard error of the mean.

Table 4
EDX analyses of the CEM-II experiments.

Areas	scale: <1 mm		Crusts	Scale:	5–25 μm	Matrices	scale:	5–25 μm	Platelets	scale:	5 μm
Atomic.%	X	± Ex	Atomic.%	X	± Ex	Atomic.%	X	± Ex	Atomic.%	X	± Ex
O	69.66	0.96	O	73.69	1.54	O	67.68	0.74	O	71.59	0.42
Na	0.10	0.02	Na	0.03	0.02	Na	0.26	0.11	Na	0.29	0.06
Mg	9.20	0.36	Mg	7.12	1.46	Mg	9.59	0.42	Mg	6.42	0.14
Al	5.03	0.20	Al	2.77	0.73	Al	5.60	0.19	Al	4.93	0.14
Si	14.00	0.49	Si	6.56	1.75	Si	14.57	0.45	Si	13.48	0.17
K	0.24	0.03	K	0.18	0.04	K	0.27	0.06	K	0.31	0.08
Ca	1.02	0.10	Ca	8.78	2.62	Ca	0.82	0.12	Ca	2.34	0.18
Fe	0.70	0.05	Fe	0.83	0.23	Fe	1.13	0.37	Fe	0.66	0.09
Mg/Si	0.66	0.02	Mg/Si	1.16	0.11	Mg/Si	0.67	0.03	Mg/Si	0.48	0.01
No. analyses	19		No. analyses	7		No. analyses	36		No. analyses	6	

X: average values, ± Ex: standard error of the mean.

samples subjected to high alkaline pore solutions (supplementary file, Fig. S5b). As well as (GI-)XRD analysis, the results can be associated with the bulk bentonite surface providing complementary information that reinforces the other analyses done. The examination of the mid-infrared spectra displayed broads and asymmetric bands owing to the reduced crystalline order and structural imperfections arising from many isomorphic substitutions.

In agreement with the (GI-)XRD analyses, the FT-IR study indicated that a mixture of authigenic trioctahedral smectites and/or Mg-rich phases were present together with the original montmorillonite, which is consistent with previous results. In the same vein, the 3706–3698 cm^{-1} bands were assigned to the stretching (υ) wavenumber of Mg-OH, which is distinctive of Mg-rich phases: chlorite-like mineral, brucite, or trioctahedral smectite. Poorly ordered M-S-H phases should not be dismissed since exhibiting a band around 3698 cm^{-1} (Nied et al., 2016). In smectite, the OH stretching region showed a slight OH band in the 3657–3650 cm^{-1} range, involving the contributions of the OH groups coordinated to different octahedral cations, mainly Al–Al–OH (Al_2OH) and Al–Mg–OH (AlMgOH). The benching (δ) vibration at 3624 cm^{-1} characteristic of the chemical bond Al_2OH (Farmer, 1974) indicated montmorillonite domains with the prevalence of octahedral substitutions. In this term, the bands at 917 ($\delta(Al_2OH)$) and 843 cm^{-1} (δ(AlMgO)) reflected substitutions of octahedral Al by Mg in montmorillonite (Madejová and Komadel, 2001; Madejová et al., 2009; Chukanov and Chervonnyi, 2016; Gates et al., 2017). The 1110, 1033 and 620 cm^{-1} bands could correspond to Si–O–Si stretching vibrations coupled to Al-O and Si-O vibrations. These bands are characteristic of montmorillonite, and serpentine, for 1032 and 788 cm^{-1} (Frost and Kloprogge, 1999). However, for these bands it is difficult to make distinctions and therefore, to establish solid conclusions. The Al^{VI}–O–Si bending band (Al^{VI}–Al in octahedral positions) appears near 520 cm^{-1} and Si–O–Si near 470 cm^{-1}. Also, the occurrence of a 575 cm^{-1} band is typical of altered samples and could be assigned to brucite and trioctahedral clay minerals (Repacholi, 2012).

4. Discussion

4.1. Areas and matrices analyses

Within each type of experiment, areas and matrices groups were significantly similar revealing the bulk perturbations of bentonite surfaces. However, significant differences were observed between the different types of experiments. It was noticeable the distinct surfaces texture and morphologies presented by CEM-II-experiments, which lies in the composition of the OPC used to make cement mortars. CEM-I and LpH are based in CEM-I OPC while in the case of CEM-II cement mortars, were made with CEM-II as OPC, characterized by the limestone addition (UNE-EN 197–1:2011). This addition increased at least the Ca content of the alkaline solution, which was ultimately reflected in the texture of the surfaces of bentonite and its chemical composition as showed in the EDX analysis. Surface characterization using (GI-)XRD, and FT-IR revealed that bentonite surface alterations of areas and matrices were higher in the CEM-II and CEM-I-experiments, with the most intense produced by high pH cement base materials in comparison with low-pH. In addition, ternary projections and the statistical survey also supported these higher Mg and Ca perturbations in CEM-I and CEM-II-experiments.

4.2. Platelets analyses

The morphology of platelets was similar in the three types of experiments. However, in terms of chemical composition they presented differences: i) platelets from LpH-experiments showed higher Al content (Fig. 7), ternary projections plotted the platelets close to references (Fig. 8) and the structural formula fitted well to an unaltered 2:1 dioctahedral smectite; thus, suggested that platelets in LpH experiments suffered lower alteration and correspond to the original montmorillonite from bentonite; ii) the platelets from the CEM-I experiments showed the highest Mg increase and could be as a consequence of the presence of trioctahedral clay minerals, mainly serpentines and pseudochlorites

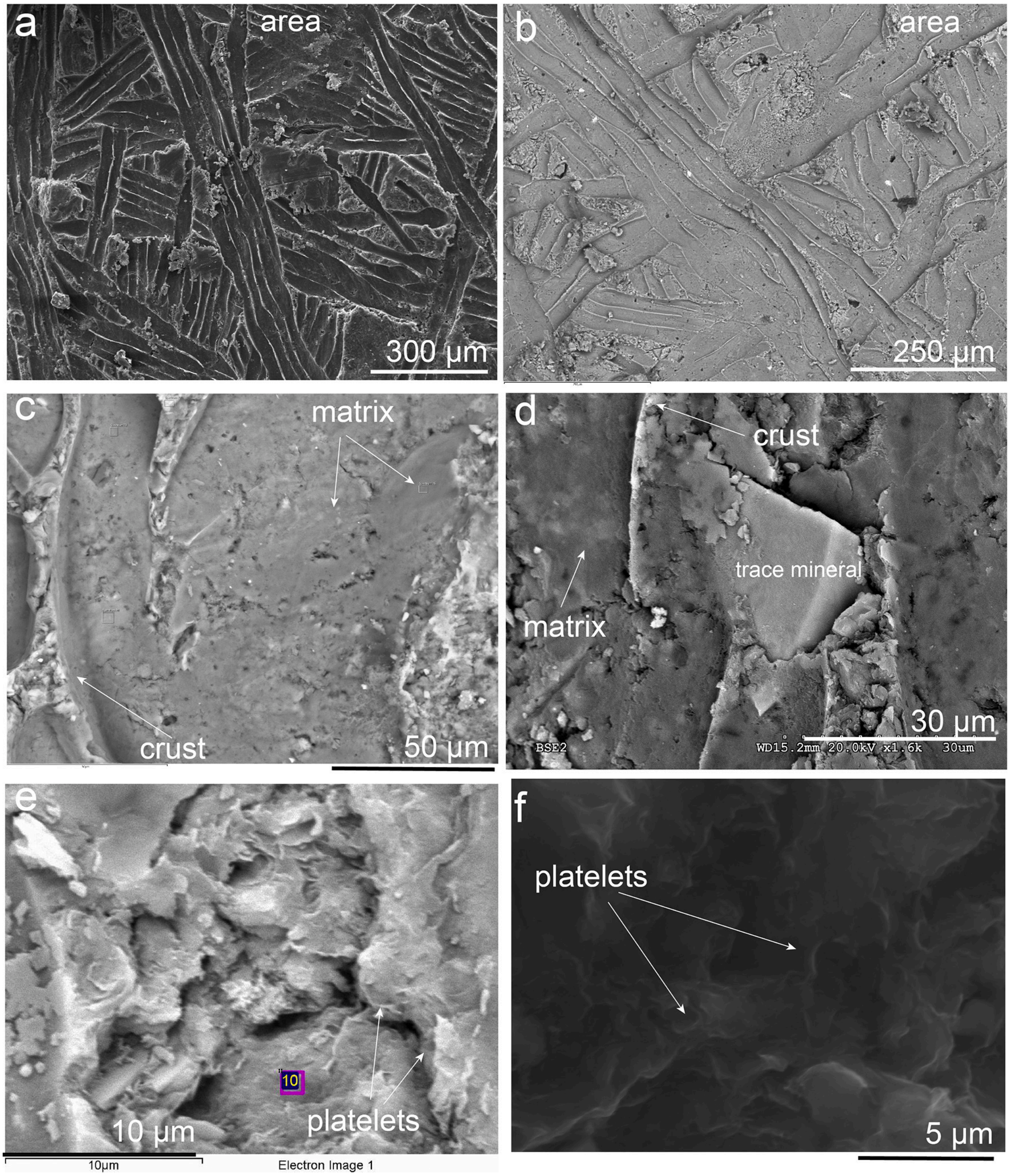

Fig. 5. SEM micrographs from the surface planes of bentonite under the influence of the CEM-II alkaline pore fluids. a) SE image of an area, b) BSE image of an area; c, d, e and f) crusts, platelets and matrices. (Trace minerals characteristic of FEBEX-bentonite were also found).

considering the structural formulas. At this point, a weakness of the calculated structural formulas lies in the fact that brucite interlayer sheets from 2:1:1 chlorite-like structures do not consider the presence of vacancies and in such case, Mg and/or Al could be located in the octahedral sheet when were present low cation occupancy. iii) platelets in CEM-II experiments match with 2:1 trioctahedral clay minerals according to the structural formulas, but this was not observed in ternary diagrams because they computed the Ca content. The lower Mg-influence over CEM-II-experiments compared with CEM-I could be associated with the negative correlation tendencies between Ca and Mg (Fig. S1, grey plots) and positive correlation between CEM-II and Ca (Fig. S1, green plots). In this sense, Dauzères et al. (2016) reported an inverse relationship between the Mg and Ca precipitation in the concrete/bentonite interface.

4.3. *Crusts analyses*

Crust-like morphologies were not present in the reference bentonite pointed to an alteration process. These crusts were presumably formed by small crystallites and aggregates which results in poorly defined morphologies formed mainly by Mg and Ca-phases. The pattern of crusts in CEM-I and LpH-experiments showed a surface with steps while CEM-II presented more homogeneous block shapes. Crusts from CEM-II-experiments presented different compositions that highlight by the greater weight of the Ca. In this term, Ca-crusts were wide extended in the surface of bentonites exposed to CEM-II alkaline solutions and were indicative of the precipitation of carbonates, presumably calcite. The formation of Ca-phases like calcite in clays exposed to alkaline solutions has been widely described in URL, laboratory experiments and natural

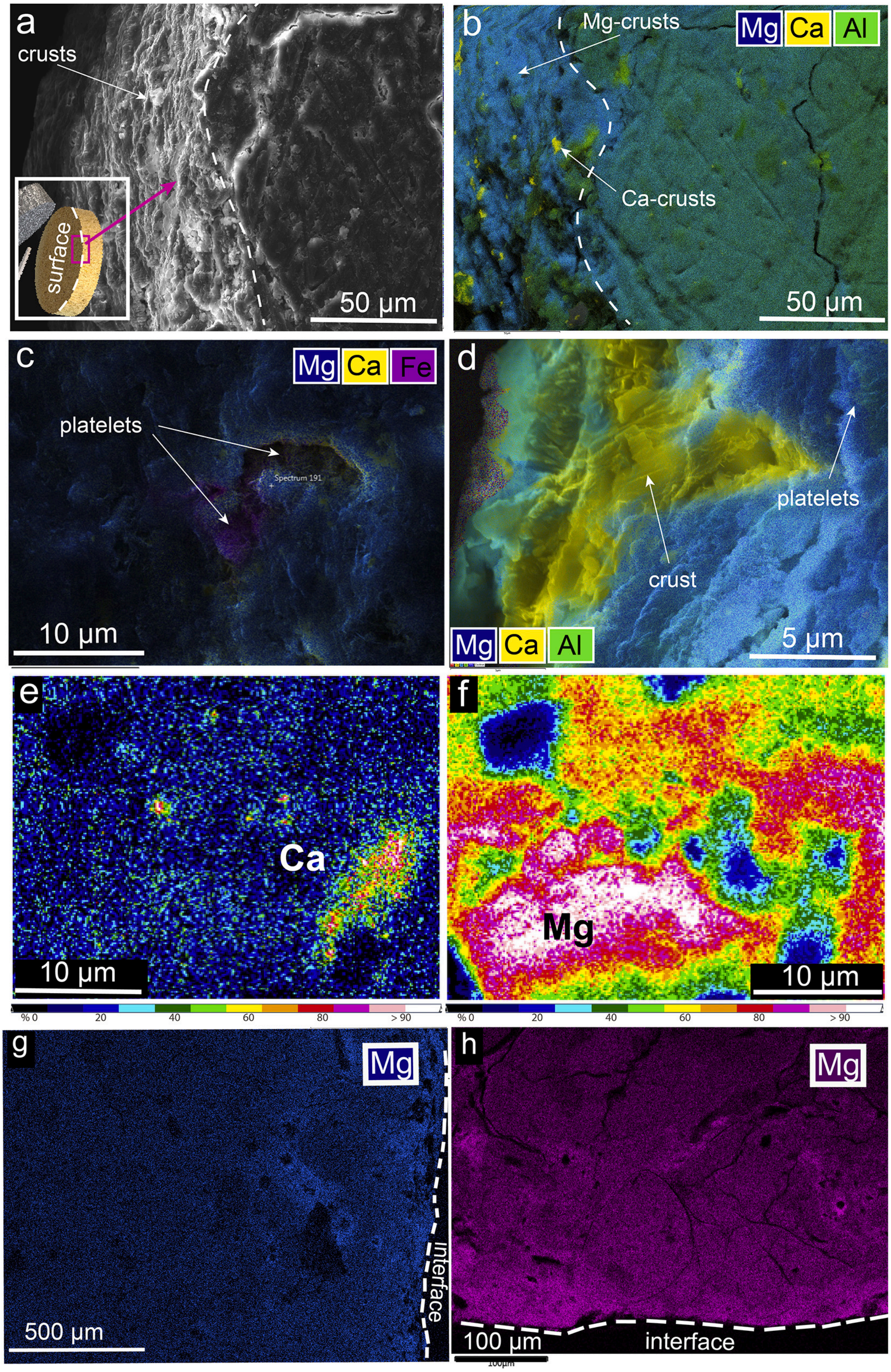

Fig. 6. SEM-EDS characterizations of the surface of bentonite and element mappings of transversally cut sections subjected to pore solutions from CEM-I as a representative example of a high pH cement mortar. a) SE image of the bentonite surface. b) Mg-Ca-Al-EDS mapping. c) Mg-Ca-Fe-EDS mapping, d) Mg-Ca-Al-EDS mapping. d) Ca-EDS mapping and f) Mg-EDS mapping of the same grid scanned. g) and h) Mg mappings next to interfaces.

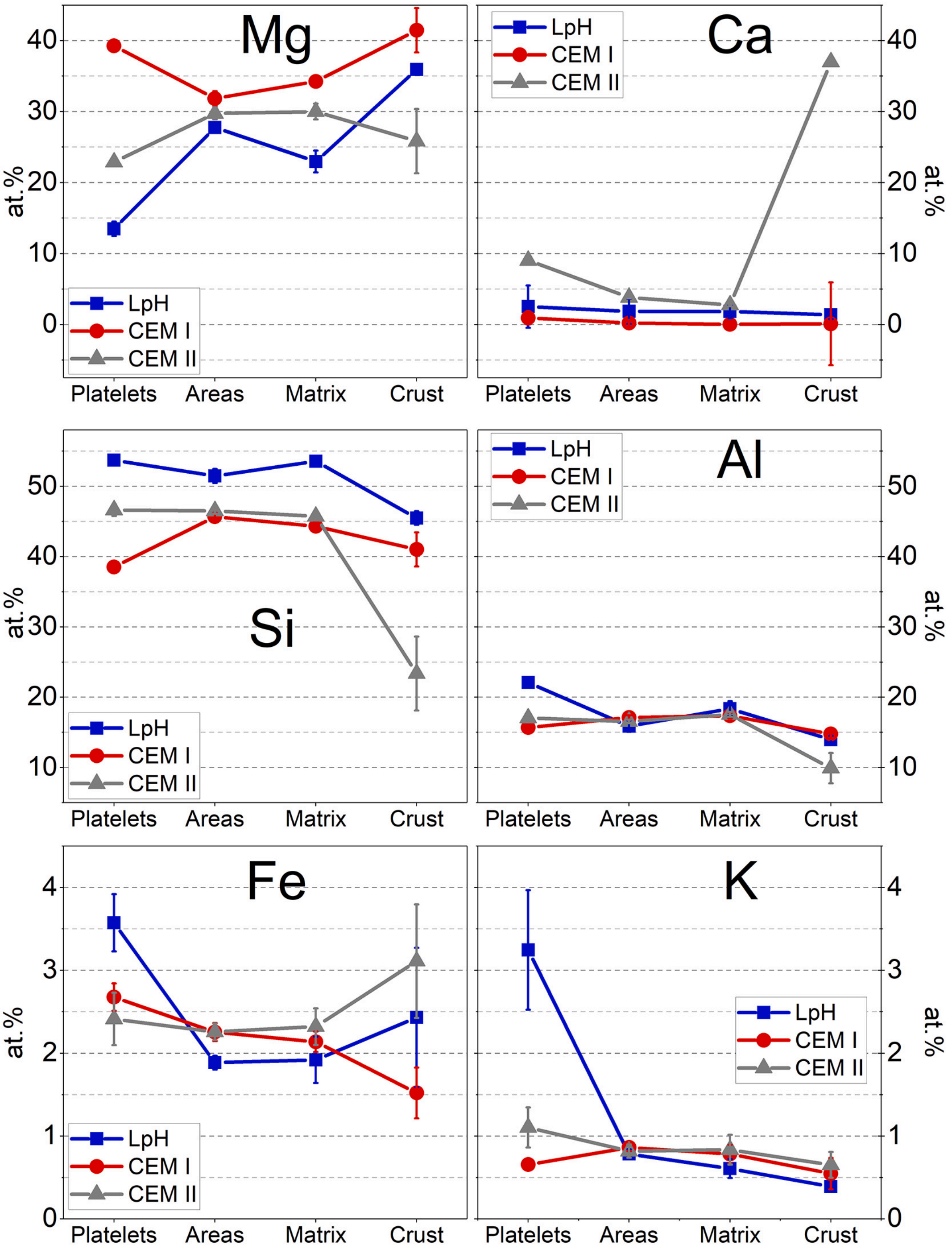

Fig. 7. Evolution of the elemental chemical composition considering the groups and experiments. The type of experiment are represented as colour lines, and the groups are represented in the X-axes. The atomic percentage (at.%) mean values obtained for Mg, Ca, Si, Al, Fe and K are represented in the Y-axes.

analogues (Fernández et al., 2017; Cuevas et al., 2018; Shimbashi et al., 2018). Moreover, tobermorite-like C-A-S-H was described in batch laboratory experiments by Fernández et al. (2016), but in this work, it was not possible to detect them due to their small crystal size, highly complex structure (Jackson et al., 2013) and the greater influence of the surrounding Mg-phases. In the CEM-I, LpH-experiments, and even CEM-II-experiments once excluding Ca from the analysis, crusts morphologies correspond to rich Mg-phases and would be formed by groups of messy small crystal size as M-S-H gels. Another more plausible possibilities are the formation of 2:1 trioctahedral clay minerals like saponite-vermiculite (Gaboreau et al., 2020). Furthermore, the presence of montmorillonite with intercalated brucite layers like a pseudochlorite structure has been previously purposed by Cuevas et al. (2018); Cuevas et al. (2019) and González-Santamaría et al. (2020b).

Regarding the origin of the Mg perturbations observed, it has been reported that alkaline solutions from cement-base materials reach the bentonite and replace partially the Mg exchangeable cations in montmorillonite being released to the alkaline medium where precipitates as Mg-rich phases such as M-S-H or brucite (Gaucher and Blanc, 2006; Lerouge et al., 2017; Cuevas et al., 2018; Fernández et al., 2018). This would be related to the Mg-rich-platelets and crusts found in the surface of bentonite as well as the Mg increases showed in the areas and matrices. In parallel, Ca-rich fluids coming from the dissolution of the hydration products of cement (mainly, portlandite and C-S-H, and the

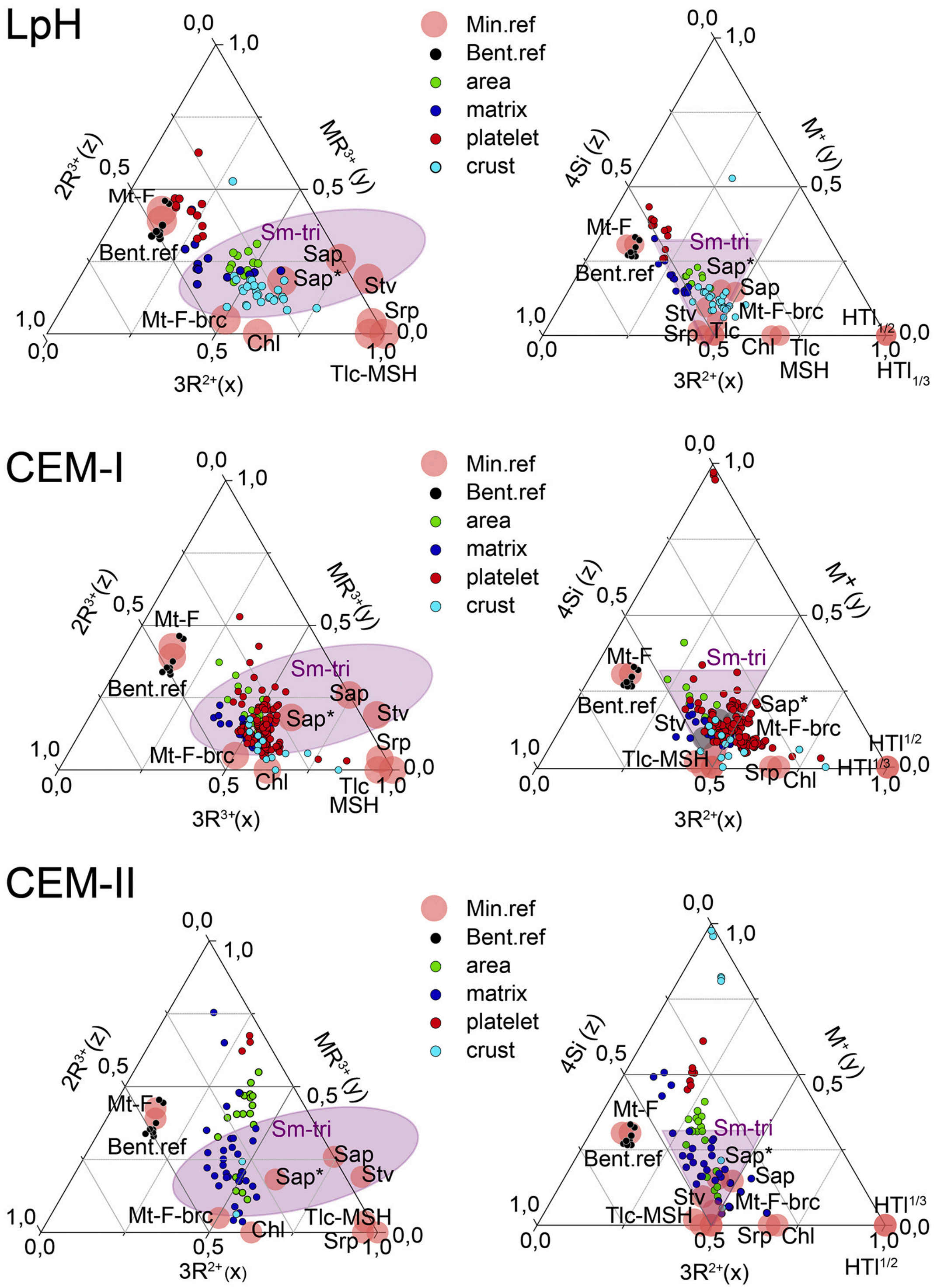

Fig. 8. Ternary diagrams of LpH, CEM-I and CEM-II-experiments. At the left is represented the MR^{3+}–$2R^{3+}$–$3R^{2+}$ ternary diagram while at the right is depicted the M^{+}–4Si–$3R^{2+}$ projection. Mt-F: montmorillonite FEBEX naturally present in unaltered FEBEX-bentonite; Bent. ref.: reference bentonite; Mt-F-bcr: montmorillonite FEBEX intercalated with brucite layers; Srp: serpentine; Stv: stevensite; Tlc: talc; Chl: chlorite; Sap and Sap*: saponite forms; MSH: magnesium silicate hydrates; HTI ½: hydrotalcite ½ Al/Mg; HTI $^{1}/_{3}$: hydrotalcite $^{1}/_{3}$ Al/Mg. Sm-tri: trioctahedral smectites. Small circular areas correspond to mineral references while large shaded areas correspond to the trioctahedral smectites previously fixed by Velde (1985).

limestone addition in the case of CEM-II) reach the bentonite where the lower pH conditions and the presence of dissolved carbonate species from bentonite pore waters drive to the precipitation of Ca-carbonates. This is consistent with the presence of Ca crust-like morphologies in high pH experiments and the isolated rich Ca sites found in element mappings.

5. Conclusions

Bentonite is a cornerstone barrier for the isolation of high-level radioactive waste within Deep Geological Repositories, then it needs to be thoroughly characterized from early stages since it may suffer alkaline perturbations in contact with cement-based materials. In this

Table 5

Structural formulas according to the type of experiment and morphology.

Exp.	Morphology	Structure	[Si	Al]^{IV}	O	[Al	Fe^{3+}	Mg]^{VI}	(OH)	Ca	Na	K	X	Oct ch.	Tet ch.	No. Oct.cat				No.an
Bent. ref	Platelets	2:1-di	3.82	0.18	10	1.39	0.13	0.56	2	0.13	0.21	0.04	0.50	−0.32	−0.18	2.08				9
		Sx	0.03	0.03		0.04	0.03	0.06		0.01	0.09	0.01	0.09	0.10	0.03	0.05				
Exp.	Morphology	Structure	[Si	Al]^{IV}	O	[Al	Fe^{3+}	Mg]^{VI}	(OH)	Ca	Na	K	X	Oct ch.	Tet ch.	No. Oct.cat				No.an
LpH	Platelets	2:1-di	3.60	0.40	10	1.08	0.24	0.90	2	0.17	0.09	0.22	0.65	−0.25	−0.40	2.22				12
		Sx	0.09	0.09	0	0.09	0.08	0.24		0.03	0.02	0.17	0.12	0.16	0.09	0.12				
LpH	Crusts	2:1-tri	3.36	0.64	10	0.36	0.12	2.48	2	0.08	0.03	0.03	0.23	0.41	−0.64	2.96				18
		Sx	0.15	0.15		0.13	0.07	0.22		0.02	0.03	0.02	0.04	0.14	0.15	0.11				
LpH	Morphology	Structure	[Si	Al]^{IV}	O	[Fe^{3+}	Mg]^{VI}	(OH)	Ca	Na	K	[Al	Mg	(OH)]	X	brc int. ch.	Tet ch.	No. Oct.cat	2:1 Oct ch.	No.an
	Crusts	2:1:1-chl. Like	3.87	0.13	10	0.23	1.97	2	0.00	0.02	0.04	1.46	1.54	6	0.05	1.46	−0.13	5.19	−1.26	6
		Sx	0.13	0.13		0.06	0.18		0.00	0.01	0.02	0.16	0.16		0.03	0.16	0.13	0.14	0.37	
Exp.	Morphology	Structure	[Si	Al]^{IV}	O	[Al	Fe^{3+}	Mg]^{VI}	(OH)	Ca	Na	K	X	Oct ch.	Tet ch.	No. Oct.cat				No.an
CEM-I	Platelets	1:1-tri	1.68	0.32	5	0.50	0.09	2.27	4	0.00	0.00	0.01	0.01	0.31	−0.32	2.86				18
		Sx	0.05	0.05		0.05	0.02	0.12		0.00	0.01	0.00	0.01	0.05	0.05	0.05				
CEM-I	Morphology	Structure	[Si	Al]^{IV}	O	[Al	Fe^{3+}	Mg]^{VI}	(OH)	Ca	Na	K	X	Oct ch.	Tet ch.	No. Oct.cat				No.an
	Platelets	2:1-tri	3.29	0.71	10	0.41	0.25	2.20	2	0.12	0.01	0.11	0.36	0.36	−0.71	2.85				16
		Sx	0.12	0.12		0.19	0.10	0.23		0.04	0.01	0.11	0.14	0.21	0.12	0.14				
CEM-I	Morphology	Structure	[Si	Al]^{IV}	O	[Fe^{3+}	Mg]^{VI}	(OH)	Ca	Na	K	[Al	Mg	(OH)]	X	brc int. ch.	Tet ch.	No. Oct.cat	2:1 Oct ch.	No.an
	Platelets	2:1:1-chl. Like	3.69	0.31	10	0.24	2.18	2	0.00	0.00	0.00	1.24	1.76	6	0.00	1.24	−0.31	5.41	0.61	52
		Sx	0.10	0.10		0.08	0.14		0.00	0.00	0.01	0.10	0.10		0.01	0.10	0.10	0.10	0.21	
CEM-I	Morphology	Structure	[Si	Al]^{IV}	O	[Fe^{3+}	Mg]^{VI}	(OH)	Ca	Na	K	[Al	Mg	(OH)]	X	brc int. ch.	Tet ch.	No. Oct.cat	2:1 Oct ch.	No.an
	Crusts	2:1: 1.chl.like	3.87	0.13	10	0.10	2.26	2	0.00	0.00	0.00	1.31	1.69	6	0.00	1.31	−0.13	5.36	0.27	2
		Sx	0.04	0.04		0.14	0.29		0.00	0.00	0.00	0.12	0.12		0.00	0.12	0.04	0.15	0.08	
CEM-I	Morphology	Structure	[Si	Al]^{IV}	O	[Al	Fe^{3+}	Mg]^{VI}	(OH)	Ca	Na	K	X	Oct ch.	Tet ch.	No. Oct.cat				No.an
	Crusts	2:1-tri	3.26	0.74	10	0.39	0.22	2.36	2	0.06	0.01	0.07	0.20	0.53	−0.74	2.96				5
		Sx	0.14	0.14		0.14	0.16	0.06		0.01	0.01	0.05	0.08	0.08	0.14	0.04				
Exp.	Morphology	Structure	[Si	Al]^{IV}	O	[Al	Fe^{3+}	Mg]^{VI}	(OH)	Ca	Na	K	X	Oct ch.	Tet ch.	No. Oct.cat				No.an
CEM-II	Platelets	2:1-tri	3.53	0.47	10	0.81	0.17	1.68	2	0.00	0.08	0.08	0.16	0.32	−0.47	2.66				6
		Sx	0.02	0.02		0.06	0.06	0.06		0.00	0.04	0.05	0.06	0.05	0.02	0.03				
CEM-II	Morphology	Structure	[Si	Al]^{IV}	O	[Fe^{3+}	Mg]^{VI}	(OH)	Ca	Na	K	[Al	Mg	(OH)]	X	brc int. ch.	Tet ch.	No. Oct.cat	2:1 Oct ch.	No.an
	Crusts	2:1:1-chl. Like	3.94	0.06	10	0.17	1.98	2.00	0.00	0.00	0.00	1.59	1.41	6	0.00	1.59	−0.06	5.15	0.13	2
		Sx	0.07	0.07	0	0.07	0.06	0.00	0.00	0.00	0.00	0.03	0.03		0.00	0.03	0.07	0.01	0.13	

Exp: experiment type, di: dioctahedral, tri: trioctahedral, Bent. ref.: reference bentonite, X: charge per half unit cell, brc int. ch: brucite interlayer charge, Oct ch.: octahedral charge, Tet. ch.: tetrahedral charge 2:1 Oct. ch.: correspond to the charge from octahedral sheet sandwiched between the two tetrahedral sheets, No. Oct. cat: total number of octahedral cations, No.an: number of analyses done, chl. Like: chlorite-like mineral structure, srp. Like: serpentine-like mineral structure.

context, compacted bentonite samples were exposed to alkaline solutions in contact with cement mortars in laboratory tests, and the morphologies formed at the bentonite surface together with their chemical composition were assessed by SEM-EDX. In addition, the study was complemented with further analytical techniques: XRD, GI-XRD, FT-IR as well as statistical analysis.

Using a SEM-EDX approach, it has been possible to recognise two morphologies patterns: platelets and crusts. Additionally, the SEM-EDX analysis made it possible to assess the bulk surface of bentonite using areas and matrices analyses under three different alkaline conditions representative of the scenarios considered for their implementation in Engineered Barrier Systems. Thus, a comprehensive morphological and semi-quantitative chemical composition description of bentonite perturbations in the early stages is provided. The study showed that the characteristics of the morphology and their composition changed depending on the solution considered allowing a quick-easy assessment of the perturbations occurring in the surface of bentonite.

In general, an increase in Mg was found in the three types of experiments being more noticeable in bentonites subjected to high pH pore fluids provided by the CEM-I and CEM-II cement mortars. This Mg alteration was more prominent in platelets and crusts morphologies and could indicate the presence of Mg-rich phases such as M-S-H, trioctahedral smectites and/or intercalated brucite layers considering the results of the XRD and FT-IR analyses. Furthermore, this Mg disturbance would be connected with the morphology of the newly formed crusts coatings, characterized by their messy appearance, which could consist of M-S-H or trioctahedral clay minerals. Furthermore, a higher Ca increase was found in bentonites exposed to pore fluids released by the CEM II Ordinary Portland Cement. This Ca increase was higher in the crust morphologies, especially in the CEM-II-experiments, these shapes could consist of mixtures of Ca-carbonates along with Mg-rich phases. However, due to the difficulty of making connections between the different morphologies characterized by SEM and the other analyses presented, further studies should be carried out at the nm scale since they would enable a more realible identification of the alteration processes involved.

The knowledge gained from this study will assist in the assessment and ongoing research of the FEBEX-bentonite performance within the Engineered Barrier Systems.

Declaration of Competing Interest

The authors declare that they have no known competing financial interests or personal relationships that could have appeared to influence the work reported in this paper.

Acknowledgements

The experimental work was supported by funding from the European Union‘s Horizon 2020 Research and Training programme from EURATOM [H2020-NFRP 2014, 2015] under grant agreement n°662147; CEBAMA.

Appendix A. Supplementary data

Supplementary data to this article can be found online at https://doi.org/10.1016/j.clay.2021.106223.

References

Apted, M.J., Ahn, J., 2017. 1 - Repository 101: multiple-barrier geological repository design and isolation strategies for safe disposal of radioactive materials. In: Apted, M.J., Ahn, J. (Eds.), Geological Repository Systems for Safe Disposal of Spent Nuclear Fuels and Radioactive Waste, Second edition. Woodhead Publishing, pp. 3–26.

Berner, U., Kulik, D.A., Kosakowski, G., 2013. Geochemical impact of a low-pH cement liner on the near field of a repository for spent fuel and high-level radioactive waste. Physics Chem. Earth A/B/C 64, 46–56. https://doi.org/10.1016/j.pce.2013.03.007.

Bleam, W., 2017. Chapter 3 - Clay mineralogy and chemistry. In: Bleam, W. (Ed.), Soil and Environmental Chemistry, Second edition. Academic Press, pp. 87–146.

Blechschmidt, I., Vomvoris, S., 2010. Underground research facilities and rock laboratories for the development of geological disposal concepts and repository systems. In: Ahn, J., Apted, M.J. (Eds.), Geological Repository Systems for Safe Disposal of Spent Nuclear Fuels and Radioactive Waste. Woodhead Publishing, pp. 82–118.

Bohor, B.F., Hughes, R.E., 1971. Scanning electron microscopy of clays and clay minerals. Clay Clay Miner. 19, 49–54. https://doi.org/10.1346/CCMN.1971.0190105.

Bouchet, A., Meunier, A., Sardini, P., 2002. Minéraux argileux: structure cristalline, identification par diffraction de rayons X., France.

Brigatti, M.F., Galán, E., Theng, B.K.G., 2013. Chapter 2 - Structure and mineralogy of clay minerals. In: Bergaya, F., Lagaly, G. (Eds.), Developments in Clay Science. Elsevier, pp. 21–81.

Brindley, G., 1980. Crystal Structures of Clay Minerals and their X-Ray Identification. Mineralogical Society, London, p. 1980.

Bristow, T.F., Milliken, R.E., 2011. Terrestrial perspective on authigenic clay mineral production in ancient Martian lakes. Clay Clay Miner. 59, 339–358. https://doi.org/10.1346/CCMN.2011.0590401.

Caballero, E., Reyes, E., Yusta, A., Puerta, F.J.H., González, J.L., 1985. Las bentonitas de la zona sur de Cabo de Gata (Almería). Geoquímica y Mineralogía. Acta geológica hispánica 267–287.

Caballero, E., Jiménez de Cisneros, C., Huertas, F.J., Huertas, F., Pozzuoli, A., Linares, J., 2005. Bentonites from Cabo de Gata, Almería, Spain: a mineralogical and geochemical overview. Clay Miner. 40, 463–480. https://doi.org/10.1180/0009855054040184.

Christidis, G., 2006. Layer charge of smectites: linking crystal structure with physical properties. Acta Crystallographica Sect. A 62, s63. https://doi.org/10.1107/S0108767306098734.

Chukanov, N.V., Chervonnyi, A.D., 2016. Infrared Spectroscopy of Minerals and Related Compounds. Springer.

Cuevas, J., Ruiz, A.I., Fernández, R., Torres, E., Escribano, A., Regadío, M., Turrero, M.J., 2016. Lime Mortar-Compacted Bentonite–Magnetite Interfaces: An Experimental Study Focused on the Understanding of the EBS Long-Term Performance for High-Level Nuclear Waste Isolation DGR Concept, pp. 124–125, 79-93. https://doi.org/10.1016/j.clay.2016.01.043.

Cuevas, J., Ruiz, A., Fernández, R., González-Santamaría, D., Angulo, M., Ortega, A., Torres, E., Turrero, M., 2018. Authigenic clay minerals from interface reactions of concrete-clay engineered barriers: a new perspective on Mg-clays formation in alkaline environments. Minerals 8, 362. https://doi.org/10.3390/min8090362.

Cuevas, J.A.M., González-Santamaría, D.E., González-Yélamos, J., Fernández, R., Ortega, A., Ruiz, A.I., 2019. High pH concrete - FEBEX bentonite interface reactions: From months to decades and from cm3 experiments to m3 in-situ scenario. In: Altmaier, M., Montoya, V., Duro, L., Valls, A. (Eds.), Proceedings of the Second Workshop of the HORIZON 2020 CEBAMA Project. KIT Scientific Publishing, Karlsruhe, pp. 125–131.

Czímerová, A., Bujdák, J., Dohrmann, R., 2006. Traditional and novel methods for estimating the layer charge of smectites. Appl. Clay Sci. 34, 2–13. https://doi.org/10.1016/j.clay.2006.02.008.

Dauzeres, A., Le Bescop, P., Sardini, P., Cau Dit Coumes, C., 2010. Physico-chemical investigation of clayey/cement-based materials interaction in the context of geological waste disposal: Experimental approach and results. Cem. Concr. Res. 40, 1327–1340. https://doi.org/10.1016/j.cemconres.2010.03.015.

Dauzères, A., Le Bescop, P., Cau-Dit-Coumes, C., Brunet, F., Bourbon, X., Timonen, J., Voutilainen, M., Chomat, L., Sardini, P., 2014. On the physico-chemical evolution of low-pH and CEM I cement pastes interacting with Callovo-Oxfordian pore water under its in situ CO2 partial pressure. Cem. Concr. Res. 58, 76–88. https://doi.org/10.1016/j.cemconres.2014.01.010.

Dauzères, A., Achiedo, G., Nied, D., Bernard, E., Alahrache, S., Lothenbach, B., 2016. Magnesium perturbation in low-pH concretes placed in clayey environment—solid characterizations and modeling. Cem. Concr. Res. 79, 137–150. https://doi.org/10.1016/j.cemconres.2015.09.002.

Dixon, J.B., 1989. Kaolin and Serpentine Group minerals. Min. Soil Environ. 467–525. https://doi.org/10.2136/sssabookser1.2ed.c10.

Elless, M.P., 1995. Mincalc1—a spreadsheet for the rapid calculation of 2: 1 phyllosilicate mineral formulae from chemical analyses. Clay Clay Miner. 43, 387–389.

Emmerich, K., Wolters, F., Kahr, G., Lagaly, G., 2009. Clay profiling: the classification of montmorillonites. Clay Clay Miner. 57, 104–114. https://doi.org/10.1346/CCMN.2009.0570110.

ENRESA, 2002. Thermo-Hydro-Mechanical Characterisation of a Bentonite from Cabo de Gata. ENRESA, Madrid. Spain, p. 258.

ENRESA, 2006. FEBEX Project Final Report Post-Mortem Bentonite Analysis. ENRESA, Madrid. Spain, p. 183.

Ewing, R.C., Whittleston, R.A., Yardley, B.W.J.E., 2016. Geological disposal of nuclear waste: a primer. Elements 12, 233–237. https://doi.org/10.2113/gselements.12.4.233.

Farmer, V.C., 1974. Infrared Spectra of Minerals. Mineralogical Society.

Fernández, A.M., Baeyens, B., Bradbury, M., Rivas, P., 2004. Analysis of the porewater chemical composition of a Spanish compacted bentonite used in an engineered barrier. Physics Chem. Earth A/B/C 29, 105–118. https://doi.org/10.1016/j.pce.2003.12.001.

Fernández, R., Vigil de la Villa, R., Ruiz, A.I., García, R., Cuevas, J., 2013. Precipitation of chlorite-like structures during OPC porewater diffusion through compacted bentonite at 90°C. Appl. Clay Sci. 83-84, 357–367. https://doi.org/10.1016/j.clay.2013.07.021.

Fernández, R., Ruiz, A.I., Cuevas, J., 2016. Formation of C-A-S-H phases from the interaction between concrete or cement and bentonite, 51, 223–235. https://doi.org/10.1180/claymin.2016.051.2.09.

Fernández, R., Torres, E., Ruiz, A.I., Cuevas, J., Alonso, M.C., García Calvo, J.L., Rodríguez, E., Turrero, M.J., 2017. Interaction processes at the concrete-bentonite interface after 13 years of FEBEX-Plug operation. Part II: Bentonite contact. Physics Chem. Earth A/B/C 99, 49–63. https://doi.org/10.1016/j.pce.2017.01.009.

Fernández, R., González-Santamaría, D., Angulo, M., Torres, E., Ruiz, A.I., Turrero, M.J., Cuevas, J., 2018. Geochemical conditions for the formation of Mg silicates phases in bentonite and implications for radioactive waste disposal. Appl. Geochem. 93, 1–9. https://doi.org/10.1016/j.apgeochem.2018.03.012.

Frost, R.L., Kloprogge, J.T., 1999. Infrared emission spectroscopic study of brucite. Spectrochim. Acta A Mol. Biomol. Spectrosc. 55, 2195–2205. https://doi.org/10.1016/S1386-1425(99)00016-5.

Gaboreau, S., Rodríguez-Cañas, E., Maeder, U., Jenni, A., Turrero, M.J., Cuevas, J., 2020. Concrete perturbation in a 13-year in situ concrete/bentonite interaction from FEBEX experiments. New insight of 2:1 Mg phyllosilicate precipitation at the interface. Appl. Geochem. 118, 104624. https://doi.org/10.1016/j.apgeochem.2020.104624.

García Calvo, J.L., Hidalgo, A., Alonso, C., Fernández Luco, L., 2010. Development of low-pH cementitious materials for HLRW repositories. Cem. Concr. Res. 40, 1290–1297. https://doi.org/10.1016/j.cemconres.2009.11.008.

García Calvo, J.L., Alonso, M.C., Hidalgo, A., Fernández Luco, L., Flor-Laguna, V., 2013. Development of low-pH cementitious materials based on CAC for HLW repositories: long-term hydration and resistance against groundwater aggression. Cem. Concr. Res. 51, 67–77. https://doi.org/10.1016/j.cemconres.2013.04.008.

Gates, W., Kloprogge, J.T., Madejova, J., Bergaya, F., 2017. Infrared and Raman Spectroscopies of Clay Minerals. Elsevier.

Gaucher, E.C., Blanc, P., 2006. Cement/clay interactions–a review: experiments, natural analogues, and modeling. Waste Manag. 26, 776–788. https://doi.org/10.1016/j.wasman.2006.01.027.

Goldstein, J.I., Newbury, D.E., Michael, J.R., Ritchie, N.W.M., Scott, J.H.J., Joy, D.C., 2017. Scanning Electron Microscopy and X-Ray Microanalysis. Springer.

Gómez-Espina, R., Villar, M.V., 2016. Time evolution of MX-80 bentonite geochemistry under thermo-hydraulic gradients. Clay Miner. 51, 145–160. https://doi.org/10.1180/claymin.2016.051.2.03.

González-Santamaría, D.E., Angulo, M., Ruiz, A.I., Fernández, R., Ortega, A., Cuevas, J., 2018. Low-pH cement mortar-bentonite perturbations in a small-scale pilot laboratory experiment. Clay Miner. 53, 237–254. https://doi.org/10.1180/clm.2018.16.

González-Santamaría, D.E., Fernández, R., Ruiz, A.I., Ortega, A., Cuevas, J., 2020a. Bentonite/CEM-II cement mortar interface experiments: a proxy to in situ deep geological repository engineered barrier system surface reactivity. Appl. Geochem. 117, 104599. https://doi.org/10.1016/j.apgeochem.2020.104599.

González-Santamaría, D.E., Fernández, R., Ruiz, A.I., Ortega, A., Cuevas, J., 2020b. High-pH/low pH ordinary Portland cement mortars impacts on compacted bentonite surfaces: application to clay barriers performance. Appl. Clay Sci. 193, 105672. https://doi.org/10.1016/j.clay.2020.105672.

Grim, R.E., 1953. Clay Miner. 76, 317.

Huertas, F.J., Carretero, P., Delgado, J., Linares, J., Samper, J., 2001. An Experimental Study on the Ion-Exchange Behavior of the Smectite of Cabo de Gata (Almería, Spain): FEBEX Bentonite. J. Colloid Interface Sci. 239, 409–416. https://doi.org/10.1006/jcis.2001.7605.

IAEA, 2012. The Safety Case and Safety Assessment for the Disposal of Radioactive Waste. IAEA.

Jackson, M.D., Chae, S.R., Mulcahy, S.R., Meral, C., Taylor, R., Li, P., Emwas, A.-H., Moon, J., Yoon, S., Vola, G., Wenk, H.-R., Monteiro, P.J.M., 2013. Unlocking the secrets of Al-tobermorite in Roman seawater concrete†. Am. Mineral. 98, 1669–1687. https://doi.org/10.2138/am.2013.4484.

Jenni, A., Mäder, U., Lerouge, C., Gaboreau, S., Schwyn, B., 2014. In situ interaction between different concretes and Opalinus Clay. Physics Chem. Earth A/B/C 70-71, 71–83. https://doi.org/10.1016/j.pce.2013.11.004.

Kaufhold, S., Dohrmann, R., 2016. Distinguishing between more and less suitable bentonites for storage of high-level radioactive waste. Clay Miner. 51, 289–302. https://doi.org/10.1180/claymin.2016.051.2.14.

Lerouge, C., Gaboreau, S., Grangeon, S., Claret, F., Warmont, F., Jenni, A., Cloet, V., Mäder, U., 2017. In situ interactions between Opalinus Clay and Low Alkali Concrete. Physics Chem. Earth A/B/C 99, 3–21. https://doi.org/10.1016/j.pce.2017.01.005.

Lothenbach, B., Le Saout, G., Ben Haha, M., Figi, R., Wieland, E., 2012. Hydration of a low-alkali CEM III/B–SiO2 cement (LAC). Cem. Concr. Res. 42, 410–423. https://doi.org/10.1016/j.cemconres.2011.11.008.

Madejová, J., Komadel, P., 2001. Baseline studies of the clay minerals society source clays: infrared methods. Clay Clay Miner. 49, 410–432.

Madejová, J., Pentrák, M., Pálková, H., Komadel, P., 2009. Near-infrared spectroscopy: a powerful tool in studies of acid-treated clay minerals. Vib. Spectrosc. 49, 211–218. https://doi.org/10.1016/j.vibspec.2008.08.001.

Mäder, U., Jenni, A., Lerouge, C., Gaboreau, S., Miyoshi, S., Kimura, Y., Cloet, V., Fukaya, M., Claret, F., Otake, T., Shibata, M., Lothenbach, B., 2017. 5-year chemico-physical evolution of concrete–claystone interfaces, Mont Terri rock laboratory (Switzerland). Swiss J. Geosci. 110, 307–327. https://doi.org/10.1007/s00015-016-0240-5.

Meunier, A., 2005. Crystal Structure — Species — Crystallisation, Clays. Springer Berlin Heidelberg, Berlin, Heidelberg.

Moore, D.M., Reynolds Jr., R.C., 1989. X-Ray Diffraction and the Identification and Analysis of Clay Minerals. Oxford University Press (OUP).

Nied, D., Enemark-Rasmussen, K., L'Hopital, E., Skibsted, J., Lothenbach, B., 2016. Properties of magnesium silicate hydrates (M-S-H). Cem. Concr. Res. 79, 323–332. https://doi.org/10.1016/j.cemconres.2015.10.003.

Nonat, A., 2004. The structure and stoichiometry of C-S-H. Cem. Concr. Res. 34, 1521–1528. https://doi.org/10.1016/j.cemconres.2004.04.035.

Norris, S., 2017. Radioactive waste confinement: clays in natural and engineered barriers – introduction. Geol. Soc. Lond., Spec. Publ. 443, 1–8. https://doi.org/10.1144/SP443.26.

Ramírez, S., Cuevas, J., Vigil, R., Leguey, S., 2002. Hydrothermal alteration of "La Serrata" bentonite (Almeria, Spain) by alkaline solutions. Appl. Clay Sci. 21, 257–269. https://doi.org/10.1016/S0169-1317(02)00087-X.

Reed, S.J.B., 2005. Electron Microprobe Analysis and Scanning Electron Microscopy in Geology. Cambridge University Press.

Repacholi, M., 2012. Clay Mineralogy: Spectroscopic and Chemical Determinative Methods. Springer Science & Business Media.

Roosz, C., Grangeon, S., Blanc, P., Montouillout, V., Lothenbach, B., Henocq, P., Giffaut, E., Vieillard, P., Gaboreau, S., 2015. Crystal structure of magnesium silicate hydrates (M-S-H): the relation with 2:1 Mg–Si phyllosilicates. Cem. Concr. Res. 73, 228–237. https://doi.org/10.1016/j.cemconres.2015.03.014.

Savage, D., 2014. An Assessment of the Impact of the Long Term Evolution of Engineered Structures on the Safety-Relevant Functions of the Bentonite Buffer in a HLW Repository. National Cooperative for the Disposal of Radioactive Waste.

Savage, D., Walker, C., Arthur, R., Rochelle, C., Oda, C., Takase, H., 2007. Alteration of bentonite by hyperalkaline fluids: a review of the role of secondary minerals. Physics Chem. Earth A/B/C 32, 287–297. https://doi.org/10.1016/j.pce.2005.08.048.

Sellin, P., Leupin, O.X., 2013. The use of clay as an engineered barrier in radioactive-waste management a review. Clay Clay Miner. 61, 477–498. https://doi.org/10.1346/CCMN.2013.0610601.

Shimbashi, M., Sato, T., Yamakawa, M., Fujii, N., Otake, T., 2018. Formation of Fe- and Mg-rich smectite under hyperalkaline conditions at Narra in Palawan, the Philippines. Minerals 8, 155. https://doi.org/10.3390/min8040155.

Taylor, H.F.W., 1997. Cement Chemistry, 2nd edition ed. Thomas Telford, London.

Tournassat, C., Steefel, C.I., Bourg, I.C., Bergaya, F., 2015. Natural and engineered clay barriers. In: Tournassat, C., Steefel, C.I., Bourg, I.C., Bergaya, F. (Eds.), Developments in Clay Science. Elsevier, pp. 1–4.

Turrero, M.J., Cloet, V., 2017. FEBEX-DP Concrete ageing, concrete/bentonite and concrete/rock interaction analysis. In: Nagra (Ed.), NAB 16-18, p. 282, 5430 Wettingen Switzerland.

Velde, B., 1985. Clay minerals (Developments in Sedimentology, Volume 40). Elsevier, Amsterdam.